Improving solar wind modeling at Mercury: Incorporating transient solar phenomena into the WSA-ENLIL model with the Cone extension

Ryan M. Dewey[1], Daniel N. Baker[1], Brian J. Anderson[2], Mehdi Benna[3], Catherine L. Johnson[4,5], Haje Korth[2], Daniel J. Gershman[6,7], George C. Ho[2], William E. McClintock[1], Dusan Odstrcil[8,9], Lydia C. Philpott[4], Jim M. Raines[6], David Schriver[10], James A. Slavin[6], Sean C. Solomon[11,12], Reka M. Winslow[4,13], and Thomas H. Zurbuchen[6]

[1]Laboratory for Atmospheric and Space Physics, University of Colorado, Boulder, Colorado, USA, [2]The Johns Hopkins University Applied Physics Laboratory, Laurel, Maryland, USA, [3]Solar System Exploration Division, NASA Goddard Space Flight Center, Greenbelt, Maryland, USA, [4]Department of Earth, Ocean and Atmospheric Sciences, University of British Columbia, Vancouver, British Columbia, Canada, [5]Planetary Science Institute, Tucson, Arizona, USA, [6]Department of Atmospheric, Oceanic and Space Sciences, University of Michigan, Ann Arbor, Michigan, USA, [7]Geospace Physics Laboratory, NASA Goddard Space Flight Center, Greenbelt, Maryland, USA, [8]Computational and Data Sciences, George Mason University, Fairfax, Virginia, USA, [9]Heliophysics Science Division, NASA Goddard Space Flight Center, Greenbelt, Maryland, USA, [10]Department of Physics and Astronomy, University of California, Los Angeles, California, USA, [11]Department of Terrestrial Magnetism, Carnegie Institution of Washington, Washington, District of Columbia, USA, [12]Lamont-Doherty Earth Observatory, Columbia University, Palisades, New York, USA, [13]Institute for the Study of Earth, Ocean, and Space, University of New Hampshire, Durham, New Hampshire, USA

Abstract Coronal mass ejections (CMEs) and other transient solar phenomena play important roles in magnetospheric and exospheric dynamics. Although a planet may interact only occasionally with the interplanetary consequences of these events, such transient phenomena can result in departures from the background solar wind that often involve more than an order of magnitude greater ram pressure and interplanetary electric field applied to the planetary magnetosphere. For Mercury, an order of magnitude greater ram pressure combined with high Alfvén speeds and reconnection rates can push the magnetopause essentially to the planet's surface, exposing the surface directly to the solar wind flow. In order to understand how the solar wind interacts with Mercury's magnetosphere and exosphere, previous studies have used the Wang-Sheeley-Arge (WSA)-ENLIL solar wind modeling tool to calculate basic and composite solar wind parameters at Mercury's orbital location. This model forecasts only the background solar wind, however, and does not include major transient events. The Cone extension permits the inclusion of CMEs and related solar wind perturbations and thus enables characterization of the effects of strong solar wind disturbances on the Mercury system. The Cone extension is predicated on the assumption of constant angular and radial velocities of CMEs to integrate these phenomena into the WSA-ENLIL coupled model. Comparisons of the model results with observations by the MESSENGER spacecraft indicate that the WSA-ENLIL+Cone model more accurately forecasts total solar wind conditions at Mercury and has greater predictive power for magnetospheric and exospheric processes than the WSA-ENLIL model alone.

1. Introduction

Modeling of solar wind conditions throughout the inner heliosphere continues to advance in capability and accuracy [e.g., *Arge et al.*, 2004; *Odstrcil et al.*, 2004a; *Pizzo et al.*, 2011; *Tóth et al.*, 2012; *Lee et al.*, 2013]. Although initially motivated in part to provide "forecasts" of upstream solar wind conditions for Earth, these models have since been applied in other studies. *Baker et al.* [2009, 2011, 2013] used these empirical and numerical modeling tools to examine the ambient solar wind at Mercury's orbital location to understand solar wind forcing of the planet's magnetospheric and exospheric processes for comparison with observations by the MErcury Surface, Space ENvironment, GEochemistry, and Ranging (MESSENGER) spacecraft. In this paper, we expand on these earlier analyses by modeling transient solar eruptions—most notably coronal mass ejections (CMEs)—in addition to the ambient solar wind to improve solar wind forecasting at Mercury's orbital location. This more complete approach provides a firmer basis on which to study magnetospheric and exospheric processes at Mercury and thereby better understand how the solar wind drives the Mercury system.

Launched in 2004, the MESSENGER spacecraft completed three flybys of Mercury in 2008–2009 before insertion into orbit about the planet on 18 March 2011. During the first Earth year of the orbital phase of the mission, the spacecraft orbited the planet with a 12 h period, typically spending 1–2 h inside the magnetosphere. With two orbit-correction maneuvers in April 2012, 1 month into MESSENGER's first extended mission, the spacecraft orbital period was shortened to 8 h. The spacecraft began its second extended mission on 18 March 2013, and orbital operations ended with planetary impact on 30 April 2015.

MESSENGER results indicate that Mercury's magnetosphere has a structure similar to that of Earth [*Johnson et al.*, 2012] in the sense that Mercury's internal magnetic field is largely dipolar with a southward polarity and is closely aligned with the planetary spin axis [*Anderson et al.*, 2008, 2010, 2012; *Alexeev et al.*, 2010]. Despite these commonalities, the strength of the internal magnetic field at Mercury's surface is only approximately 1% that at Earth [*Anderson et al.*, 2010, 2012]. As a result, whereas Earth's subsolar magnetopause stands at 10–11 Earth radii from the center of the planet, Mercury's subsolar magnetopause stands only at approximately 1.5 Mercury radii [*Winslow et al.*, 2013]. This weaker intrinsic field, exposure to the highly dynamic space environment, and extremely strong average solar wind conditions [e.g., *Korth et al.*, 2011a, and references therein] result in more extreme magnetospheric fluctuations. Mercury is more responsive to changes in the interplanetary magnetic field (IMF), with time scales of 2–3 min [*Slavin et al.*, 2009, 2010], in contrast to the 40–60 min time scale at Earth [*Baker et al.*, 1996]. Magnetic reconnection rates are also ~3 times higher than typical rates at Earth [*DiBraccio et al.*, 2013], and intense solar wind ram pressure combined with high Alfvén speeds and reconnection rates can counteract the effects of induced planetary currents and allow the magnetopause to approach or even reach the planetary surface [*Winslow et al.*, 2013; *Slavin et al.*, 2014]. Magnetohydrodynamic (MHD) simulations suggest that this extreme loading occurs 6–7% of the time [*Blomberg and Cumnock*, 2004].

Interaction between the solar wind and magnetopause drives plasma processes within Mercury's magnetosphere and is dominated by the effects of reconnection [*Belenkaya et al.*, 2013]. Most prominently, the solar wind forcing leads to well-understood motion of individual particles from the reconnection of interplanetary and planetary magnetic field lines at the magnetopause [see *Korth et al.*, 2011a, 2011b, 2012; *Raines et al.*, 2012, and references therein]. The $\mathbf{E} \times \mathbf{B}$ drift resulting from reconnection, where $\mathbf{E}$ and $\mathbf{B}$ are the local electric and magnetic field vectors, respectively, substantially heats plasma and planetary material and is greater than that at Earth because of the smaller curvature of drift paths at Mercury [*Delcourt et al.*, 2002; *Zelenyi et al.*, 2007]. This reconnection effectively taps the solar wind electric field, driving the convection of magnetic flux [*Korth et al.*, 2012]. Solar wind interaction with the magnetopause and bow shock also produces a variety of wave phenomena [e.g., *Boardsen et al.*, 2012; *Sundberg et al.*, 2012, 2013; *Le et al.*, 2013] and is the primary source of energy for Mercury's magnetosphere [*Vasyliunas*, 2013]. With a strong dependence on the solar wind and IMF, Mercury's magnetosphere can experience changes in conditions on time scales of seconds to months from temporal changes in solar wind parameters [*Johnson et al.*, 2012]. Continuous knowledge of upstream solar wind conditions is therefore important to understanding and interpreting the plasma processes within Mercury's magnetosphere. Furthermore, because CMEs often involve the application to the magnetosphere of ram pressures and electric fields more than an order of magnitude greater than normal [*Slavin et al.*, 2014], modeling only the background solar wind is insufficient to represent magnetospheric processes at Mercury fully.

In earlier work [*Baker et al.*, 2009, 2011, 2013], we simulated background solar wind conditions using heliospheric modeling appropriate to the times of the three Mercury flybys and first 9 months in orbit by the MESSENGER spacecraft in 2008–2009 and 2011, respectively. To investigate the consistency and overall validity of the heliospheric modeling techniques, the first two studies [*Baker et al.*, 2009, 2011] propagated the solar wind conditions past 1 AU and compared the modeled conditions with measurements by the Advanced Composition Explorer (ACE) and the Solar TErrestrial RElations Observatory (STEREO) pair of spacecraft. Those studies indicated that the modeling provides a generally good representation of the inner heliosphere, including high-speed solar wind streams, corotating interaction regions, IMF sector boundaries, and heliospheric current sheet properties. From comparisons with MESSENGER observations, the studies also indicated that the modeling produces generally accurate conditions at Mercury's orbital location. *Baker et al.* [2013] expanded the analysis of the first two studies by examining a longer time interval (9 months versus three isolated days) and by using the model results to order and organize MESSENGER observations of magnetospheric and exospheric processes at Mercury. In that work, these observations were taken as "effectiveness" indicators to test
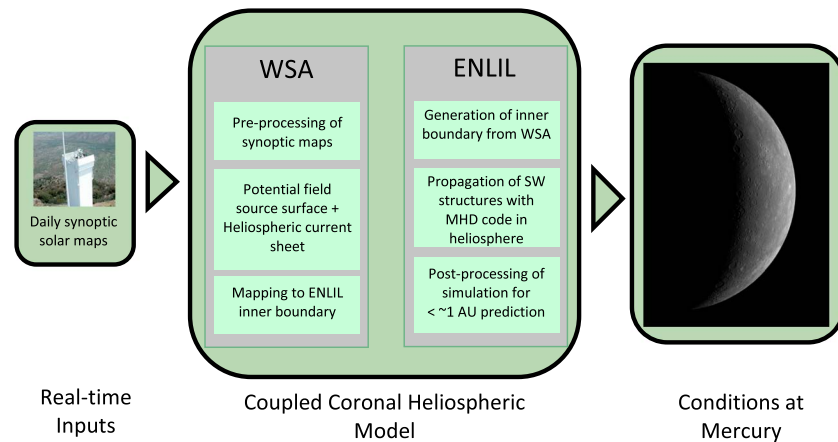
Figure 1. The observational and modeling elements that constitute the Wang-Sheeley-Arge (WSA) and ENLIL tools used in this study to model upstream background solar wind (SW) conditions. Adapted from *Baker et al.* [2013].

further the validity of the modeled conditions and as examples of how heliospheric modeling can aid planetary studies [see *Baker et al.*, 2013, and references therein]. *Baker et al.* [2013] concluded that heliospheric modeling generally provides continuous and broadly accurate upstream parameters of the background solar wind for Mercury's orbital location.

In this study, we model transient solar eruptions in addition to the background solar wind for the purpose of testing and improving solar wind forecasting at Mercury's orbital location. We compare available MESSENGER observations with the upstream solar wind parameters of the previous ambient solar wind model and with those of the updated total solar wind model during the period from March 2011 to December 2012 to identify improvements and limitations of the newer, total solar wind model. We follow much of the same procedure and format as those described by *Baker et al.* [2009, 2011, 2013], but we explicitly account for CMEs and other transient solar phenomena. We begin with a summary of our modeling techniques and brief overview of MESSENGER instruments in section 2. Methodologies include the earlier basic model, which simulates only background solar wind, and the updated model that includes CMEs and other energetic phenomena. Section 3 provides detailed results for both models for MESSENGER's first seven Mercury years in orbit. We first compare the results from the new model with available upstream MESSENGER measurements and the results from the previous model for the approximately 20 month period of analysis. We then examine particular CME events to assess how well the updated model captures transient solar phenomena. Finally, in section 4, we further compare the accuracy and validity of the new model against the earlier one by examining magnetospheric and exospheric effectiveness indicators with both models.

2. Numerical Modeling and In Situ Data Sources

To simulate the total solar wind in the inner heliosphere, we used a series of coupled empirical and numerical models in which we treated the corona and heliosphere separately. The Wang-Sheeley-Arge (WSA) model predicts coronal conditions and allows for the eventual mapping of the background solar wind. An extension of the original *Wang and Sheeley* [1992] model, WSA is a semiempirical model based on magnetic flux-tube expansion [*Arge and Pizzo*, 2000]. The model uses magnetic synoptic maps of the solar surface as input to a potential field source surface (PFSS) model that provides an estimate of current sheet properties [*Schatten et al.*, 1969]. The PFSS model is predicated on the assumption that the corona is current-free between the photosphere and 2.5 R_{sun}, beyond which the plasma controls the magnetic field, where R_{sun} is the solar radius. At 2.5 R_{sun}, all magnetic field lines are constrained to be open and radial, and the magnetic field is computed from a scalar potential that obeys Laplace's equation. With empirical relationships for magnetic flux-tube expansion, the model initializes the solar wind flow by propagating the plasma-controlled current sheet properties to 21.5 R_{sun}. These WSA outer boundary conditions become the inner boundary conditions for the heliospheric model ENLIL (Figure 1).
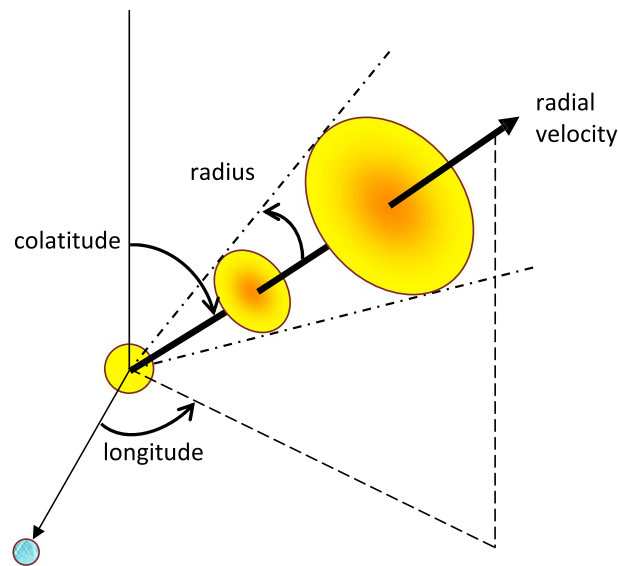
Figure 2. Coronal mass ejection (CME) geometry and propagation assumed for use of the Cone extension in modeling transient events with the WSA-ENLIL tools.

To propagate solar wind structure and evolution to 1.7 AU, we used the ideal magnetohydrodynamic (MHD) simulation ENLIL [*Odstrcil*, 2003; *Odstrcil et al.*, 2004b]. ENLIL is a time-dependent, ideal-fluid approximation to a three-dimensional model for which equal temperatures and densities are assumed for electrons and protons and microscopic processes are neglected. The computational domain grid spans 30°–150° in heliospheric colatitude, 0°–360° in longitude, and 0.1 AU (21.5 R_{sun}) to 1.7 AU in radial distance. ENLIL specifies the solar wind velocity (**V**), plasma density (*n*), mean plasma temperature (*T*), and IMF (**B**) throughout the computational domain. From these basic parameters, we determined such composite parameters as the Alfvén Mach number (M_A) and dynamic solar wind pressure ($P_{dyn} = \rho V^2$, where $\rho = nm$ and *m* is the proton mass). The combined WSA-ENLIL modeling thus provides numerical predictions of the upstream ambient solar wind for Mercury's orbital location. Although we used WSA-ENLIL to model solar wind conditions in this study, it is worth noting that alternative solar wind models have also been developed [e.g., *Hakamada and Akasofu*, 1982; *Tóth et al.*, 2005, 2012; *Feng et al.*, 2014].

To model CMEs and other solar energetic particle events in addition to the background solar wind, we used the Cone tool in conjunction with WSA-ENLIL. Cone is an iterative graphic tool that uses a cone shape to estimate initial CME parameters from white-light coronagraph images of the CME [*Zhao et al.*, 2002; *Xie et al.*, 2004]. From observations, a CME expands radially outward with constant angular width and radial direction and speed to first order [see *Zhao et al.*, 2002, and references therein; *Howard et al.*, 1982; *Fisher and Munro*, 1984], allowing the cone shape to provide a basis for estimating its initial radial speed, size, location, and direction of propagation (Figure 2). The cone-shaped CME is then integrated into WSA-ENLIL for its evolution with the background solar wind by adding a pressure pulse at the inner ENLIL boundary parameterized by the Cone-derived radial speed, angular width, source location, and direction of propagation, as well as the time at which the CME front crosses 21.5 R_{sun} [see *Lee et al.*, 2013]. ENLIL uses hydrodynamic ejecta, so the simulated CMEs are not initially configured with magnetic-cloud structure, although their extent suggests the eventual occurrence of such structures. Likewise, the cone-shaped parameterization from the coronagraph images does not initialize other plasma parameters of the CME, namely, density and temperature. The initial CME density and temperature are free parameters and are by default equal to 4 times and 1 time the typical ambient fast-wind mean values, respectively [*Mays et al.*, 2015]. These parameters can be modified so that a modeled CME matches 1 AU in situ observations more accurately. Since CMEs are integrated into the ENLIL numerical grid along with the background solar wind conditions, CMEs evolve along with the background solar wind, allowing for acceleration or deceleration of the CMEs.

We simulated 766 CMEs or other solar particle events with this WSA-ENLIL+Cone (WEC) model over our period of study. These events were all of those seen in the inner heliosphere during this period, as detected by the STEREO and/or Solar and Heliospheric Observatory spacecraft, although not all events interacted with the Mercury system. Since Cone parameters are determined analytically, there is some subjectivity and uncertainty in fitting and initializing these events [see *Lee et al.*, 2013]. On a statistical basis, modeling total solar wind conditions at Mercury's orbital location is reliable and insensitive to the uncertainty in CME parameters because of the number of events modeled and the proximity of Mercury to the inner ENLIL boundary.

To model the total solar wind, photospheric magnetic maps served as the primary input into the coupled models. These synoptic maps were constructed from magnetograms supplied by the National Solar Observatory's Global Oscillation Network Group (GONG) data set. *Baker et al.* [2013] used a static background,
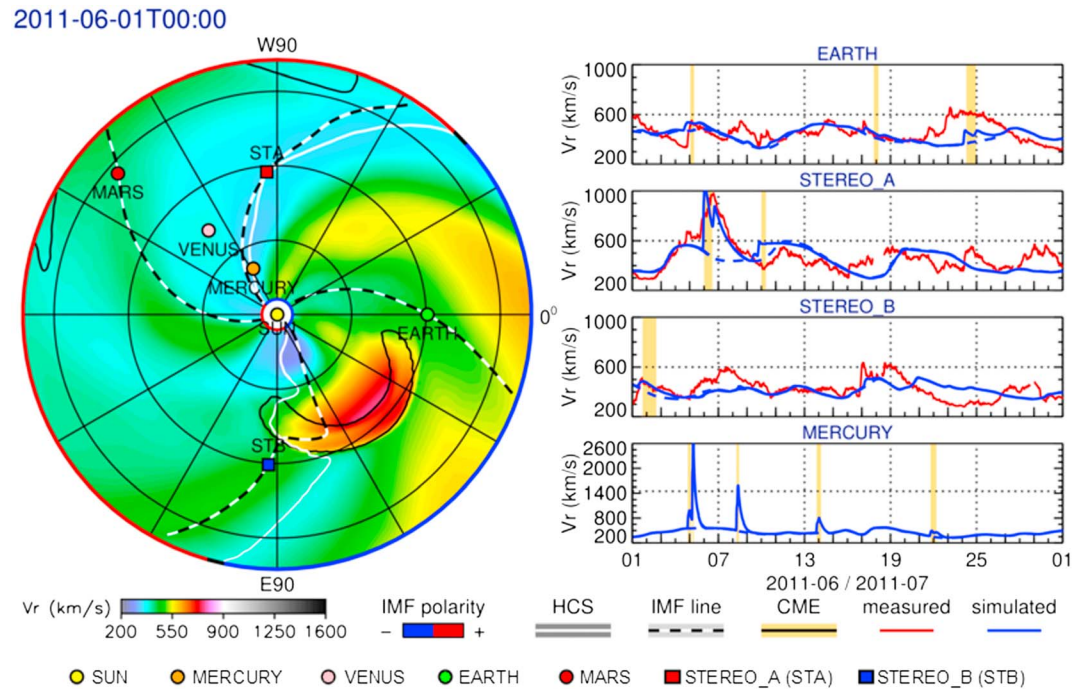
Figure 3. Modeled radial solar wind speed, viewed from the north ecliptic pole, in the ecliptic plane from the WEC model for 1 June 2011. The scale for V_r is given by the color bar. The locations of spacecraft, planets, and the Sun are indicated by small symbols. The inner boundary of the model (where WSA outputs are used) is denoted by the central circle filled in white. Other features are listed in the legend. The plots at right give V_r as simulated (blue; solid line is WEC and dashed is WSA-ENLIL) and measured (red) at Mercury, Earth, and the STEREO spacecraft for the month of June 2011. The shaded yellow areas indicate the CMEs, as incorporated into the ENLIL results with the Cone extension.

in which data from GONG were updated at a 24 h cadence; one coronal WSA map was used, and it corotated in time. Because synoptic maps were unchanged within each 24 h period, solar wind parameters experienced artificial jumps in the temporal profile with each new map, reflecting the updated photospheric conditions. For this study, we instead used an evolving background that linearly interpolates between WSA maps at 1 day cadence to provide a more continuous representation.

As in our earlier work, we have used an outer ENLIL boundary past Earth's orbital location to enable us to compare the model's results at multiple spatial locations as a validation of the model's capability. As an example, a color representation of the radial component of the solar wind velocity (V_r) in the heliospheric plane on 1 June 2011 from the WEC model is shown in Figure 3. For this example case, the model results depict fast-moving CMEs near Earth and a moderate solar wind stream region in the ecliptic plane during this time. According to the model, the ~550 km/s stream passed Earth several days prior to the snapshot but had yet to envelop STEREO-A, and the Earth had yet to interact with the energetic particles. The in situ observations from the ACE, STEREO-A, and STEREO-B spacecraft at Earth and at several longitudes in the figure match well with the prediction and capture much of the disturbed conditions. The Cone extension (yellow) captures the disturbed conditions at STEREO-A on 7 June particularly well compared with the WSA-ENLIL model only (dashed blue line). Such confirmation at a variety of locations within the inner heliosphere indicates that the solar wind conditions are predicted well by the model, as illustrated in Figure 3. Thus, we find that the WEC model does a satisfactory job of characterizing the solar wind near, behind, and ahead of Earth locations at 1 AU as seen by these three spacecraft over our period of study. For a more detailed discussion of the performance of WSA-ENLIL at 1 AU, see *Lee et al.* [2009], *Baker et al.* [2009, 2011], and *Jian et al.* [2011].

In conjunction with the WEC and WSA-ENLIL model results, we used measurements from several MESSENGER spacecraft instruments. In particular, we relied on MESSENGER's Magnetometer (MAG) [*Anderson et al.*, 2007], the Neutron Spectrometer (NS) sensor on the Gamma-Ray and Neutron Spectrometer instrument [*Goldsten et al.*, 2007], and the two sensors on the Energetic Particle and Plasma Spectrometer instrument [*Andrews*
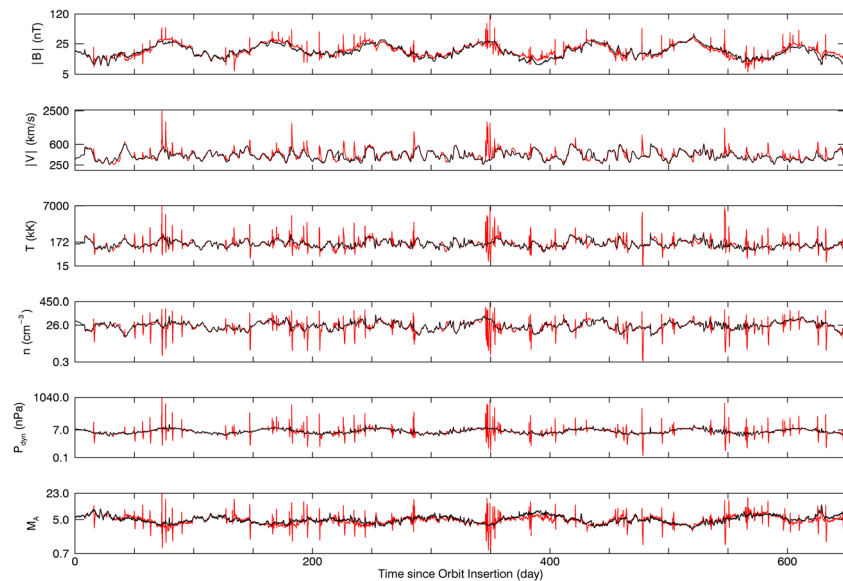
Figure 4. WEC (red) and WSA-ENLIL (black) model results at Mercury for the period of March 2011 through December 2012. Computed values of B, V, n, T, P_{dyn}, and M_A are shown in the top to bottom plots, respectively, and are displayed with logarithmic vertical scaling.

et al., 2007]: the Energetic Particle Spectrometer (EPS) and the Fast Imaging Plasma Spectrometer (FIPS) [*Zurbuchen et al.*, 1998; *Andrews et al.*, 2007]. Although MAG operated nearly continuously from 23 March 2011 to the end of the MESSENGER mission, FIPS could not often sample the majority of the solar wind distribution since the MESSENGER sunshade obstructed a direct view of the Sun. New statistical retrieval methods [*Raines et al.*, 2011; *Gershman et al.*, 2012] have greatly compensated for this limitation, however, and have increased the accuracy and frequency of FIPS solar wind observations.

3. Solar Wind Modeling Results and Basic Parameter Comparison

3.1. General Parameter Comparison

Numerical predictions for solar wind conditions from both WEC and WSA-ENLIL modeling over the period of study are shown in Figure 4. The upper four plots show the following computed parameters: IMF strength (B), solar wind speed (V), mean temperature (T), and plasma density (n), respectively. The bottom two plots show the composite parameters, dynamic solar wind pressure (P_{dyn}) and Alfvén Mach number (M_A). It is important to note the similarities between the two models. As expected, respective parameters from the two models correlate strongly with each other. The WEC model, however, captures both the ambient solar wind and departures caused by solar transient events, identifiable as spikes in the parameters in Figure 4. The plots are scaled logarithmically to highlight the agreement between the WEC and WSA-ENLIL models for the background solar wind and to display the departures from the background solar wind caused by transient solar events. Extreme solar events modeled by the Cone extension can result in an order of magnitude increase for T and P_{dyn} and 0.5 order of magnitude increase for V and n compared with the ambient parameter strength.

The parameters in Figure 4 show several obvious features. Both WSA-ENLIL and WEC model results show variations with heliospheric distance as Mercury moves in its eccentric orbit. Most apparent in the first (B) and fifth (P_{dyn}) panels, there is clear periodicity in the computed values. As expected, the period corresponds to Mercury's 88 day orbital period about the Sun. With a relatively high orbital eccentricity of 0.21, Mercury's heliocentric distance d varies from 0.31 AU to 0.47 AU, changing the solar wind conditions at the planet. As both the IMF strength and solar wind density fall off with solar distance as $\sim d^{-2}$, Mercury experiences large variations in these parameters during a Mercury year.

Throughout the period of study, the values of V and T are closely correlated with each other in both models. Density tends to anticorrelate with V (and by extension T), a result of the conservation of momentum flux in the model [see *Lee et al.*, 2013]. Likewise, the Alfvén Mach numbers are anticorrelated with the dynamic
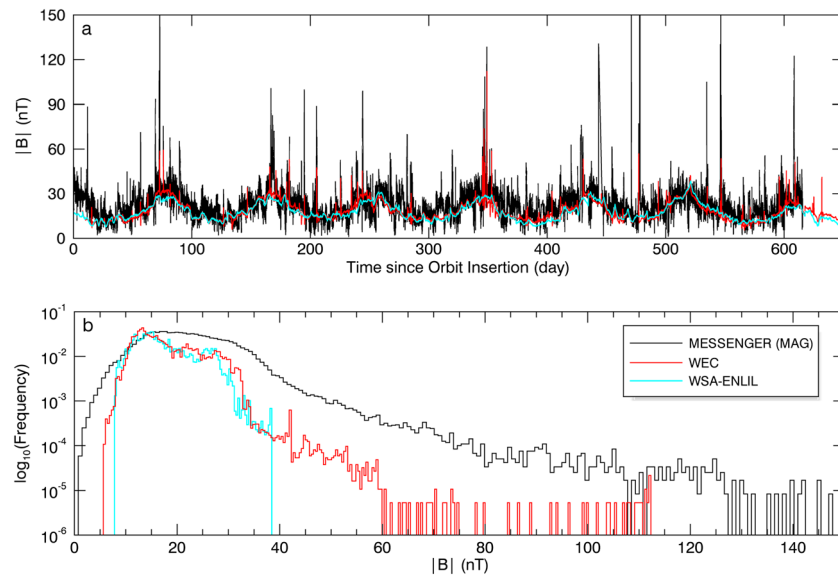
Figure 5. (a) Comparison of MESSENGER interplanetary magnetic field observations (black) with WEC (red) and WSA-ENLIL (cyan) model results over the period of analysis. The MAG data have been averaged over 5 min bins to match the time resolution of the models. (b) Histograms of the results from Figure 5a for IMF strength B.

pressure and magnetic field strength, a result that follows directly from the definition of M_A. As examined by *Baker et al.* [2009, 2011], the shorter-period (10–20 day) variations in V, T, and n are due to solar wind stream structures, such as those evident in Figure 3.

A comparison of the measured and modeled IMF strength is shown in Figure 5. Figure 5a depicts the observed and modeled IMF strength B over the period of study, and Figure 5b contains histograms of these data. The MESSENGER data shown include MAG measurements only when the spacecraft was upstream of the Mercury bow shock. We note the good agreement between the baseline values of both models with the MAG values in Figure 5a; weighted, binned correlations between the model and MAG baseline values (within three standard deviations of the mean) averaged over the ENLIL time resolution (~5 min) produce a correlation coefficient of $r = 0.95$ for both models. Although there is considerable variance in the observed field strength, both models display the long-term trends, but only the WEC model captures the transient events characterized by spikes in the field strength. As described by *Baker et al.* [2013], these transient events can last for several days, and the magnetic field magnitude during disturbed conditions can often exceed $B = 40$ nT. Although many of the CMEs and transient events were present in the WEC model, not all were captured. Organizing the IMF data in Figure 5b, we see the accuracy of the 40 nT cutoff described by *Baker et al.* [2013]. The maximum B modeled by WSA-ENLIL was 38.4 nT, suggesting that 40 nT is a good approximate cutoff for large-scale transient events.

In Figure 5b, we see close agreement between WEC and WSA-ENLIL model results about the baseline IMF ($B \approx 20$ nT), which match the observed IMF strength well. The WEC model, as one would expect, matches IMF observations better than the WSA-ENLIL model for larger B since WEC incorporates transient phenomena, but the model appears to cut off near 60 nT and reaches a maximum at 112 nT. Comparing the entire distributions, the average B modeled by WEC to the average B observed by MESSENGER is $B_{WEC}/B_{MAG} = 0.90$, whereas $B_{WSA-ENLIL}/B_{MAG} = 0.88$. We expect a higher ratio for the WEC model because of the inclusion of CMEs in the model, but the transient nature of CMEs and other eruptive events reduces their effect in long-term statistical comparisons. As predicted by WEC, B greater than 40 nT occurs at Mercury less than 0.5% of the time. Although the effect of incorporating transient events in a long-term comparison is small, it is significant; the correlation coefficient between B_{MAG} and $B_{WSA-ENLIL}$ is $r = 0.471$, but including disturbed conditions with the Cone extension increases the coefficient to $r = 0.490$ between WEC results and MESSENGER observations.

Comparing the IMF results with those from other studies, the modeling of IMF strength at Mercury's orbital location is improved compared with modeling at 1 AU. *Lee et al.* [2009] compared several 3-D MHD models
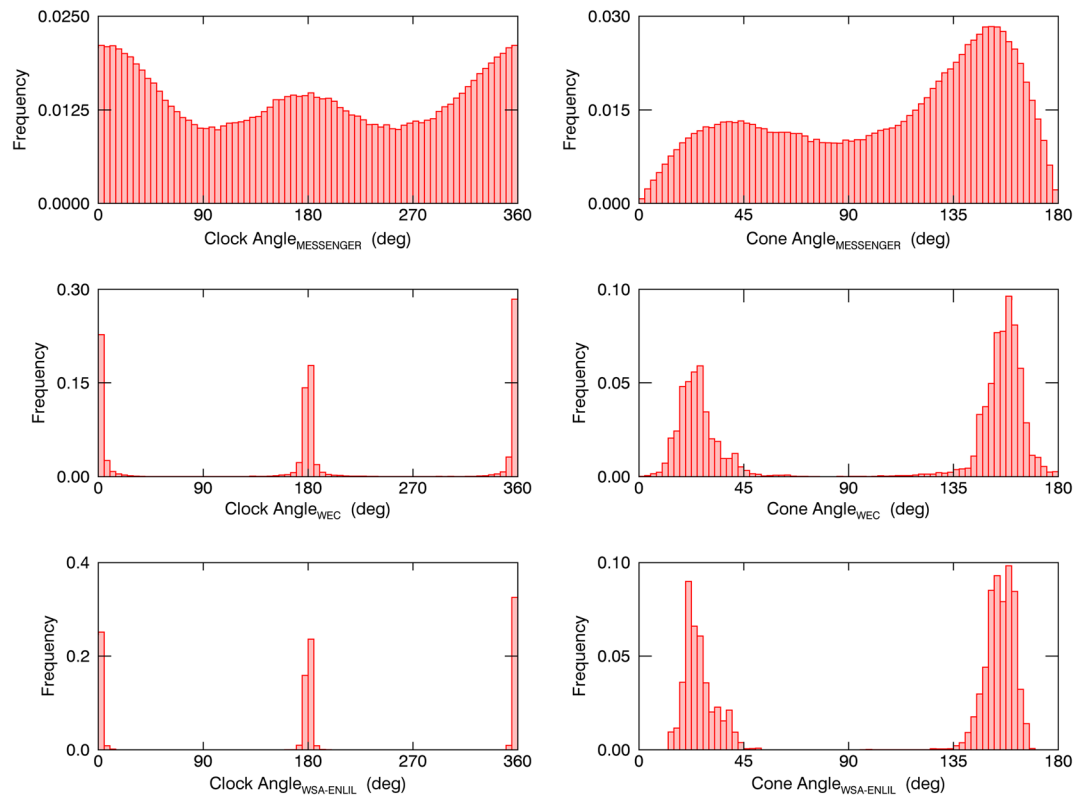
Figure 6. Distributions of the IMF (left column) clock angle and (right column) cone angle as measured by (top row) MESSENGER and simulated by the (middle row) WEC and (bottom row) WSA-ENLIL models. Clock angles of 0°, 90°, 180°, or 270° indicate that the component of the IMF perpendicular to the Sun-Mercury line points dawnward, northward, duskward, or southward, respectively.

with ACE observations at 1 AU during the declining phase of solar cycle 23 from January 2003 to January 2006. Their study used a previous version of ENLIL (see Methodologies section), but by comparing the IMF strength modeled by WSA-ENLIL with that observed by ACE, *Lee et al.* [2009] found that the average B ratio is $B_{WSA-ENLIL}/B_{ACE} \sim 0.5$. In contrast, as noted above, the ratios between WEC and MESSENGER and between WSA-ENLIL and MESSENGER are larger by nearly a factor of 2. More recently, *Gressl et al.* [2013] tested the performance of several solar wind models at 1 AU over the year 2007, a year chosen to reduce the influence of CMEs because it coincided with a period of low solar activity. Their study tested the performance of WSA-ENLIL against ACE and Wind observations and found that the modeled IMF strength correlated with the observed strength at $r = 0.18$. In contrast, the correlations between WEC and MESSENGER and between WSA-ENLIL and MESSENGER, as noted above, are much higher. The improvement of WEC and WSA-ENLIL near 0.4 AU compared with 1 AU is not unexpected; modeling the solar wind conditions at Mercury's orbital location is closer to the inner ENLIL boundary and to where the solar wind conditions are initialized.

To complete the IMF analysis, we show in Figure 6 the distributions of IMF clock angle (the angle of rotation of the IMF around the Sun-Mercury line) and cone angle (the angle between the IMF direction and the Sun-Mercury line) over the period of analysis for both model results and MESSENGER observations. MESSENGER observed a symmetric, bimodal distribution of clock angle most heavily populated at low dawn and dusk angles. The distribution of angles is also symmetric about the north-south line. These findings are consistent with the low Parker spiral angle of ~20° at Mercury [*Le et al.*, 2013]. Both WSA-ENLIL and WEC models match this bimodality, although intermediate angles are sparsely populated since ENLIL does not treat turbulent fluctuations. The WEC model better reflects the observed distribution with a higher relative frequency of northward and southward angles, but the distribution is still strongly bimodal.

The cone angle follows a similar trend between the model results. A cone angle of 0° corresponds to a magnetic field pointed radially from the Sun and an angle of 90° to a field perpendicular to the Sun-Mercury line. MESSENGER observed a bimodal distribution with peaks at ~40° and ~150°. Unlike the clock angle, the
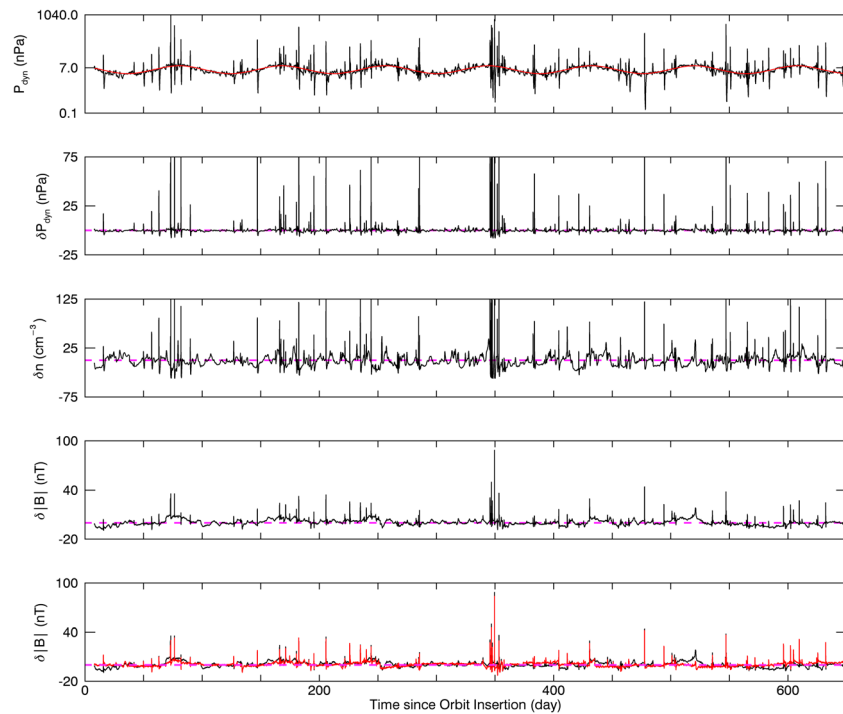
Figure 7. WEC model results at Mercury for the period of March 2011 through December 2012. (first panel) P_{dyn} from the WEC model along with an annual variation (red) derived from Mercury's orbital elements. (second to fourth panels) The WEC-modeled dynamic pressure, density, and magnetic field strength after the corresponding annual variations have been removed (such residual parameter values are denoted by the δ symbol). The dashed magenta lines indicate the zero reference levels. (fifth panel) The δB_{WEC} (black) and the magnetic field strength generated purely from the Cone extension (red, calculated from $B_{WEC}-B_{WSA-ENLIL}$).

MESSENGER cone angle distribution is less symmetrically filled, with a heavy skew to the latter peak and a low frequency of radially aligned field angles (0° or 180°). Both models capture the bimodality of the distribution, although both have more extreme bimodal characteristics than the MAG results. The WEC model again better populates the intermediate angles and more accurately reflects the skew toward the ~150° peak. IMF angles are an important component of solar wind forcing since they often dominate magnetic reconnection at the magnetopause. Recent studies of Mercury suggest, however, that the magnetic reconnection rate at Mercury is independent of clock angle [*DiBraccio et al.*, 2013].

For consistency with the analysis of *Baker et al.* [2013] and because of the powerful trends in solar wind parameters, we have removed the annual periodicity from the model results (Figure 7). The first panel in the figure contains the WEC dynamic solar wind pressure (see Figure 4 above) and the annual variation that depends solely on Mercury's eccentric orbit. The smooth curve closely follows the general pressure values with the exception of CMEs. The following three plots show variations in the residual WEC dynamic pressure (δP), density (δn), and IMF magnitude (δB), i.e., the model parameters with the lowest-frequency oscillations removed. After such removal, the CMEs simulated by the WEC model are more evident. In the final plot, we compare the WEC residual IMF magnitude δB with the results purely from the Cone extension by subtracting the WSA-ENLIL IMF magnitude results. Because the WSA-ENLIL model contains the background solar wind, and IMF strength at Mercury is largely dominated by the planet's orbit, the close match between the two curves indicates that the residual IMF magnitude is dominated by transient solar phenomena, as we might expect.

3.2. CME Event Comparisons

To compare the in situ and predicted parameters more closely, we compare the two models with MAG and FIPS measurements for several specific CME events. First, in Figure 8, we compare the models and MESSENGER observations for CME events in late November 2011. During the period 13 to 26 November 2011, MESSENGER observed several CME events at Mercury, most notably on 14, 18, 19, and 23 November. Both models accurately reflect the general background solar wind conditions over this period, although
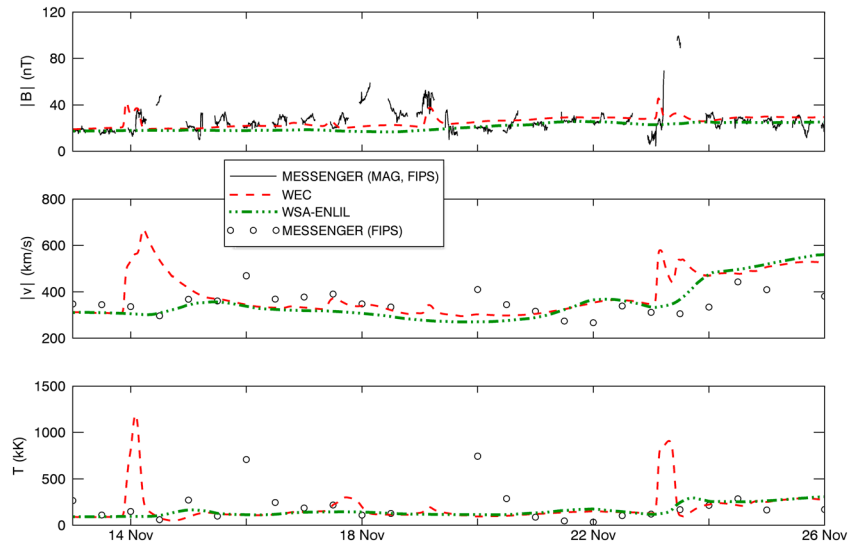
Figure 8. Solar wind parameter comparison for the November 2011 CME events at Mercury. IMF B, solar wind V, and T are shown from top to bottom. Each panel includes MESSENGER observations (MAG for B and FIPS for V and T) in black, WEC results in red, and WSA-ENLIL results in green. MAG data and models have a 5 min time resolution, whereas FIPS has a 12 h resolution because of the limitations of the instrument and statistical methods (see text). Because of the FIPS cadence, FIPS measurements are represented as back circles instead of a continuous curve. Although MAG measures the magnetic field at a much finer time resolution (between 2 to 40 samples per second), we calculated 5 min averages to match the ENLIL cadence. Gaps in the MAG data correspond to times when MESSENGER was inside Mercury's magnetosphere, and gaps in FIPS data correspond to times when the statistical retrieval methods to estimate solar wind speed and temperature were not valid.

the solar wind displayed variability on shorter time scales than the model results. Compared with the WSA-ENLIL model, the WEC model reflects the elevated solar wind speed and temperature parameter profiles of the first event (14 November), although the WEC model does not predict the arrival time of the CME at MESSENGER correctly. The WEC model also predicts an elevated IMF strength for each of the events, although the model B is weaker than the MAG observations for each event. In their study of extreme solar wind conditions at Mercury, *Slavin et al.* [2014] investigated MESSENGER observations of the 23 November 2011 event. For all three MESSENGER-measured parameters (B, V, and P_{dyn}), the WEC model substantially outperforms the WSA-ENLIL model in parameter estimation (Table 1). For that event, however, the WEC model predicts the CME 0.34 days (8 h) early and at only 45% of the observed B strength. Solar wind ram pressure is in much stronger agreement; the WEC model predicts an average ram pressure of 54.6 nPa compared with the MESSENGER-derived pressure of 51.0 nPa; and the WSA-ENLIL model, in contrast, predicts 8.0 nPa.

We next compare the models with spacecraft observations for a series of CME events in May 2012. In a pattern similar to the November 2011 events, several CMEs and other transient phenomena interacted with the Mercury system in early to mid-May, most notably the 8 May event in Figure 9. The lack of FIPS solar wind measurements over this period prevents direct comparison of the models with solar wind conditions such as solar wind speed and temperature, but as evident from the IMF strength, both models underestimate the general background solar wind conditions. Compared with the WSA-ENLIL model, the WEC model reflects the elevated IMF strength

Table 1. Solar Wind and IMF Parameters for the 23 November 2011 and 8 May 2012 CME Events

| CME Event Date	Parameter	MESSENGER[a]	WEC	WSA-ENLIL
23 Nov 2011	B (nT)	99.1	44.8	23.1
	V (km/s)	450	488	338
	P_{dyn} (nPa)	51	54.6	8
8 May 2012	B (nT)	43.4	27.8	13.8
	V (km/s)	500	310	250
	P_{dyn} (nPa)	65.1	15.4	5.4

[a]Solar wind speed and ram pressure determined by *Slavin et al.* [2014].
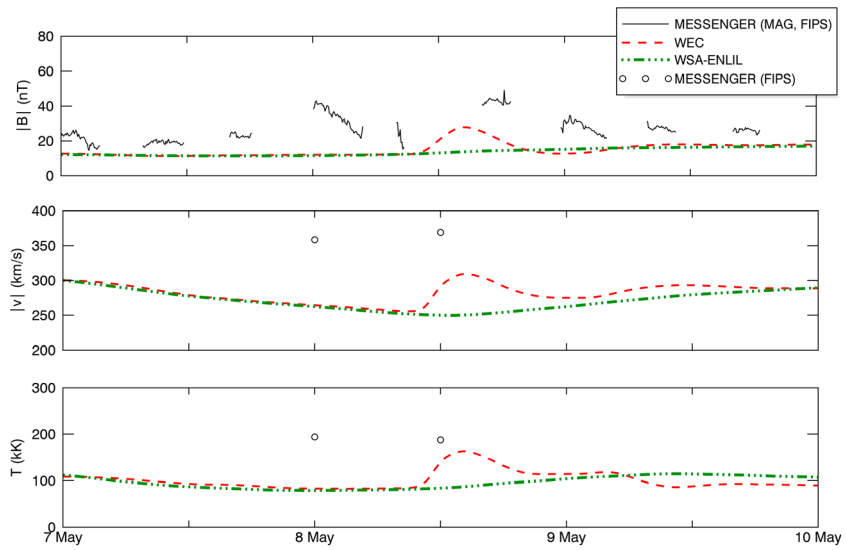
Figure 9. Solar wind parameter comparison for the 8 May 2012 CME event at Mercury in the same format as Figure 8.

for the 8 May event, although the WEC model *B* is weaker than the MAG observations for the event. Because MESSENGER crossed Mercury's magnetopause at approximately 12:00 UTC on 8 May, we cannot determine how accurately WEC predicted the CME arrival time at Mercury. *Slavin et al.* [2014] also investigated the upstream solar wind conditions for this event, and for all three MESSENGER-measured parameters, the WEC model substantially outperforms the WSA-ENLIL model in parameter estimation (Table 1). The WEC model predicts the CME at only 64% the observed magnetic strength, however, and does not predict the solar wind velocity or ram pressure for this event as well as for the 23 November event. Likewise, the WSA-ENLIL model also predicts the event conditions less accurately for this event than for the 23 November event, but the WEC model outperforms the WSA-ENLIL model for estimating parameters for this event.

The misprediction of CME arrival time and underprediction of CME magnetic strength noted above for the November 2011 and May 2012 events are typical of WEC model results. To expand the statistical description
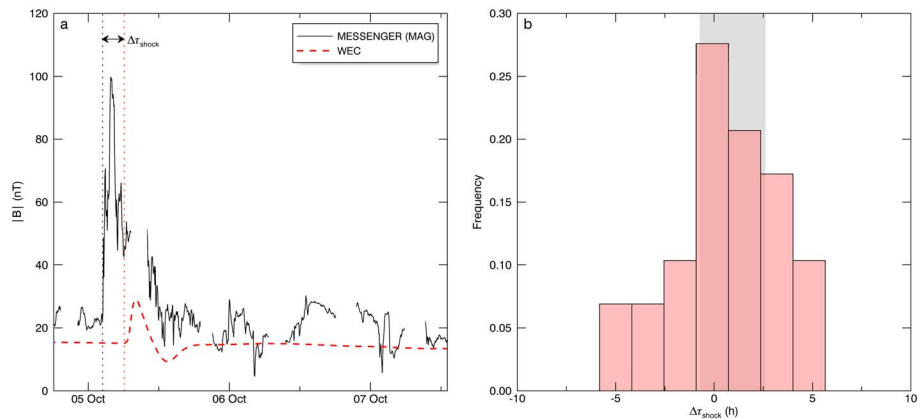
Figure 10. (a) The 5 October 2011 CME, an example of how the difference in predicted and observed CME shock arrival time was determined. The black curve corresponds to 5 min averaged MAG data, and the black dotted line corresponds to the CME shock as identified by the spacecraft. The dashed red curve corresponds to the WEC results, and the red dotted line corresponds to the CME shock as predicted by WEC. The difference in time between these two dotted lines is the error in shock arrival time, $\Delta\tau_{shock}$. The error is positive if the model predicted the shock arrived later than was observed. (b) Distribution of differences between the predicted and observed CME shock arrival times at Mercury's orbital location for 30 events modeled with WEC. The mean difference is 0.94 ± 1.67 h (see text). The grey shaded region indicates the 95% confidence interval for the mean $\Delta\tau_{shock}$.

of how accurately WEC captures the shock arrival time and CME magnetic strength, we identified 30 CMEs and related events modeled by WEC that were well recorded by MAG. We selected only CMEs for which MAG observed both a clear shock and the peak magnetic strength of the event. The 5 October 2011 event, shown in Figure 10a, provides an example of our selection criteria and how we identified the CME shock. By comparing the time difference between the shock as observed in MAG records and the shock predicted by WEC, we determined the error in shock arrival time (SAT), $\Delta\tau_{\text{shock}}$. Figure 10b shows a histogram of the SAT errors at Mercury's orbital location for the 30 identified events. The SAT error is positive if the model predicted that the shock arrived later than was observed. Although there is a considerable spread in the misprediction of arrival time, on average the WEC model mispredicts the CME arrival by only 0.94 ± 1.67 h, suggesting that there is no large or systematic offset in CME arrival time prediction over the period of study. In addition to the arrival time misprediction, the WEC model forecasts the magnetic field strength of these events at (67.8 ± 12.7)% of the observed value. This systematic underprediction of IMF strength is likely the result of not incorporating a CME magnetic field or cloud in the WEC model.

CME arrival time, although an important parameter, is challenging to predict accurately [see *Fry et al.*, 2003; *Lee et al.*, 2013]. At Earth, the arrival of an interplanetary shock and its associated CME can trigger a geomagnetic storm and other related space weather consequences, so predicting SAT accurately is critical for reliable space weather prediction. Multiple techniques have consequently been developed, and efforts made, to improve SAT prediction at Earth. *Fry et al.* [2003], for instance, compared an ensemble of shock propagation models to find an average root-mean-square (RMS) error in the SAT of approximately 12 h; *Feng et al.* [2009] introduced a database method for predicting the arrival of shocks at Earth; and *Rouillard et al.* [2009] analyzed a solar storm using multiple spacecraft at different heliocentric distances to improve our understanding of how accurately we can forecast CME features from white-light images. By procedures similar to those of this study, *Taktakishvili et al.* [2011] used the WSA-ENLIL model with the Cone extension and ACE spacecraft observations to analyze the shock arrival time of 20 CMEs at 1 AU, and they found an RMS error in the SAT of approximately 8 h. At Mercury, accurate SAT prediction is similarly necessary if the WEC model is to be used to build reliable solar wind estimates because of the strong effects CMEs and their shocks can have on the Mercury system [see *Slavin et al.*, 2014]. From the 30 identified CME shocks, we found that WEC predicts an average RMS error in the SAT of 3.1 h at Mercury's orbital location. At an average heliospheric distance of 0.39 AU, WEC's prediction at Mercury is improved over the 8 to 12 h RMS error at 1 AU, as expected. As the SAT provides a measure of how well a solar wind model can capture and predict the temporal variability of the solar wind, the Cone extension to the WSA-ENLIL model captures CME timing well, at least compared with forecasts at Earth's orbital location.

4. Magnetospheric Effectiveness Indicators

The model results presented above suggest that the WEC model predicts total solar wind conditions more accurately at Mercury than does the WSA-ENLIL model alone for the period from March 2011 onward and is thus an improvement over earlier modeling [*Baker et al.*, 2013]. Given the instrumental and orbital limitations in obtaining continuous solar wind measurements at Mercury—in situ measurements could be made only when MESSENGER was outside and upstream of the planet's bow shock—and the strong magnetospheric dependence on solar wind conditions, WEC modeling provides improved solar wind conditions for studying magnetospheric and exospheric processes at Mercury.

To assess further the accuracy and predictability of the models, we correlated modeled solar wind parameters with several magnetospheric metrics. In particular, we selected phenomena in or characteristics of Mercury's magnetosphere with which we have experience at Earth. From knowledge of how such phenomena operate at Earth, we may postulate those solar wind or IMF parameters that are most important in the driving of these phenomena at Mercury. We can then test the performance of the solar wind models at Mercury by comparing how well the parameters from each model can organize MESSENGER observations of the phenomena. The selected magnetospheric phenomena are thus "effectiveness indicators" of the predictability of each model for magnetospheric and exospheric processes. We selected magnetospheric boundary locations, magnetospheric fluctuations, and energetic particle intensity as effectiveness indicators.

For example, from studies at Earth, we know that the solar wind velocity largely determines the locations of the bow shock and magnetopause [*Shue et al.*, 1997]. Extending this result to Mercury, we can correlate the simulated velocities with the magnetopause location at Mercury's subsolar point to find the model that yields
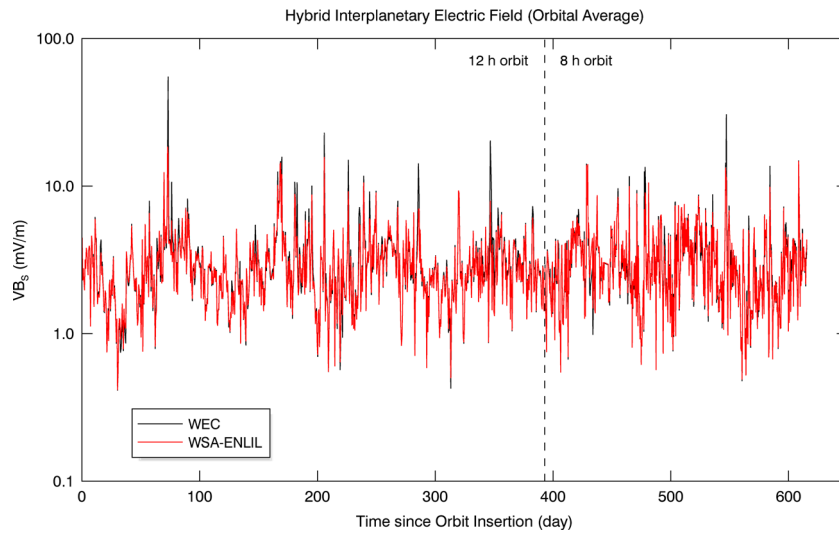
Figure 11. The hybrid index VB_S computed from ENLIL-derived estimates of the solar wind speed V and MAG measurements of the southward IMF component B_S from orbit insertion to the end of December 2012. The black curve uses WEC V values, and the red curve uses WSA-ENLIL values. The index is averaged over the orbital period of each mission phase (see text); the dashed line marks the change in MESSENGER's orbit period from 12 to 8 h.

the stronger correlation. Several of the solar wind and IMF parameters that we might assume a priori that would control the Mercury system are shown in Figure 4.

We also used the general level of magnetic activity within Mercury's magnetosphere as an assessment tool for the models. *Anderson et al.* [2012] analyzed magnetic field fluctuations within the magnetosphere from MESSENGER MAG observations and defined a magnetic disturbance index (MDI) for different levels of activity. We examined both "high-frequency" (periods of 2–20 s) and "low-frequency" (periods of 20–300 s) wave power fluctuations.

In addition to these indicators, we know from experience at Earth that the interplanetary electric field $\mathbf{E}_{IMF}$ drives substorms and many aspects of magnetospheric dynamics [e.g., *Baker et al.*, 1996]. Although ENLIL models do not directly predict the electric field, we may compute this field from $\mathbf{E}_{IMF} = -\mathbf{V}_{SW} \times \mathbf{B}_{IMF}$. Results to date indicate that WSA-ENLIL modeling produces a reliable estimator of $\mathbf{V}_{SW}$ (see section 3), one that is improved by the Cone extension. As depicted in Figure 6, however, this modeling does not produce reliable IMF angles, a recognized limitation of the model. Because of these limitations, we used a "hybrid" approach and combined the most current IMF parameter measurements by the MAG instrument on MESSENGER with WSA-ENLIL solar wind parameters. Such IMF measurements, of course, are available only when the spacecraft is outside of Mercury's magnetosphere. Although we do not have continuous measurements of the IMF, we have measurements for extended portions of each 12 h or 8 h orbit, varying by MESSENGER's orbital mission phase. To estimate the interplanetary electric field, we calculated the hybrid parameter V (ENLIL) B_S (MESSENGER) = VB_S, where B_S is the southward component of the IMF.

The hybrid forcing index VB_S computed over the period of study is shown in Figure 11. In keeping with the above description of IMF measurements, the figure shows the electric field averaged over the orbital period of MESSENGER at that time. Consistent with the results of *Baker et al.* [2013] and as expected, the Mercury system appears subjected to a range of solar wind forcing conditions extending over several orders of magnitude in the forcing index. Also as expected, the Cone extension systematically increases this forcing index and its variability, especially when CMEs interact with the Mercury system. The average VB_S of the WEC model is 3.3 mV/m, and the standard deviation in that figure is 5.3 mV/m, compared with the WSA-ENLIL mean of 3.0 mV/m and standard deviation of 3.1 mV/m. Since CMEs and related transient phenomena interact with the Mercury system on time scales shorter than the orbital period, our averaging downplays departures from the WSA-ENLIL model during such events. For smaller averaging intervals, the effect of such events is more noticeable and can increase the forcing index by another order of magnitude.

Table 2. Correlation Coefficients Between Effectiveness Indicators and Modeled Solar Wind Parameters[a]

Modeled Parameter		Effectiveness Indicator		
		Magnetopause Standoff Distance	Magnetic Disturbance Index	Neutron Spectrometer Count Rate
IMF (B)	Total	−0.98 (−0.31)	0.60 (0.16)	0.74 (0.05)
	Ambient	−0.98 (−0.29)	0.59 (0.09)	0.37 (0.02)
Velocity (V)	Total	−0.67 (−0.13)	0.70 (0.27)	0.60 (0.11)
	Ambient	−0.45 (−0.04)	0.58 (0.12)	0.42 (0.09)
Temperature (T)	Total	−0.41 (−0.14)	0.60 (0.28)	0.44 (0.10)
	Ambient	−0.73 (−0.16)	0.54 (0.13)	0.56 (0.10)
Density (n)	Total	−0.76 (−0.19)	−0.37 (−0.18)	−0.44 (−0.11)
	Ambient	−0.81 (−0.18)	−0.26 (−0.09)	−0.30 (−0.06)
Electric field (VB_S)	Total	(−)	0.85 (0.02)	(−)
	Ambient	(−)	0.86 (0.02)	(−)

[a]"Total" and "ambient" correspond to the WEC and WSA-ENLIL modeled parameters, respectively. The parenthetical values are for correlations with raw data, and values without parentheses are for correlations with binned data, as discussed in the text.

We discuss in greater detail each effectiveness indicator (magnetopause standoff distance, magnetic disturbance index, and electron events) against IMF and solar wind parameters in the subsections that follow. Each correlation was calculated between WEC or WSA-ENLIL model parameters and the primary data-derived indicator. For each specific pairing of a parameter and an indicator, we provide correlation coefficients for both the "raw" model parameter and for a weighted, binned parameter for which the weight of each bin is the number of indicator values within the bin. Binning smoothes the relations between indicators and model parameters and greatly (albeit artificially) increases the correlation strength. To reduce the artificial effects of smoothing, we kept the same histogram bin size for the WEC and WSA-ENLIL correlations. Table 2 lists the correlation coefficients associated with each of the parameter-indicator pairings.

4.1. Magnetosphere Boundary Locations: Magnetopause Standoff Distance

We used the subsolar magnetopause standoff distance (R_{SS}) calculated in the manner described by *Winslow et al.* [2013] as the first indicator. We selected only magnetopause crossings that satisfied $X_{MSO} \geq -2.0\ R_M$ in Mercury solar orbital (MSO) coordinates, where R_M is Mercury's radius, to reduce inaccuracies from the magnetopause flaring parameter. In MSO coordinates, $+X$ is toward the Sun, $+Y$ is duskward, and $+Z$ is northward. Figure 12 depicts correlations between the standoff distance (in units of R_M) and ENLIL-derived solar wind velocity (V). Figure 12a depicts the solar wind velocity from the WEC model, and Figure 12b depicts the velocity from the WSA-ENLIL model. The two figures show the correlations with both the unbinned and binned velocity values. We note that from the thousands of MESSENGER crossings the magnetopause distances are quite scattered, but both models order the data fairly well. The WEC model provides marked improvements over the standard WSA-ENLIL model, however, as it significantly improves the correlations of standoff distance both with unbinned ($r = -0.13$ versus -0.04, respectively) and binned ($r = -0.67$ versus -0.45, respectively) velocity values. We would expect the WEC model to produce a stronger correlation, given that strong forcing events can push the magnetopause to the planet's surface (see above). The other solar wind or IMF parameters we investigated (e.g., B, T, and n) do not show significant differences between the models on the basis of correlations of standoff distances with unbinned parameters. Unbinned IMF strength values from both models show moderate correlations, which we might expect from the correlation between solar wind speed and magnetic field during solar transient events and perhaps as well because the boundary crossings were determined from MAG data.

4.2. Magnetospheric Fluctuations: Magnetic Disturbance Index

We show comparisons of several modeled solar wind and IMF parameters with the low-frequency MDI in Figure 13. The WEC model improves the correlations of low-frequency MDI with all of the unbinned solar wind and IMF model parameters (B, V, T, and n). Importantly, Figure 13a shows a strong correlation between the low-frequency MDI and ENLIL velocities, and WEC significantly improves the correlation coefficients for both the unbinned and binned model parameters over WSA-ENLIL, from $r = 0.12$ to 0.27 and $r = 0.58$ to
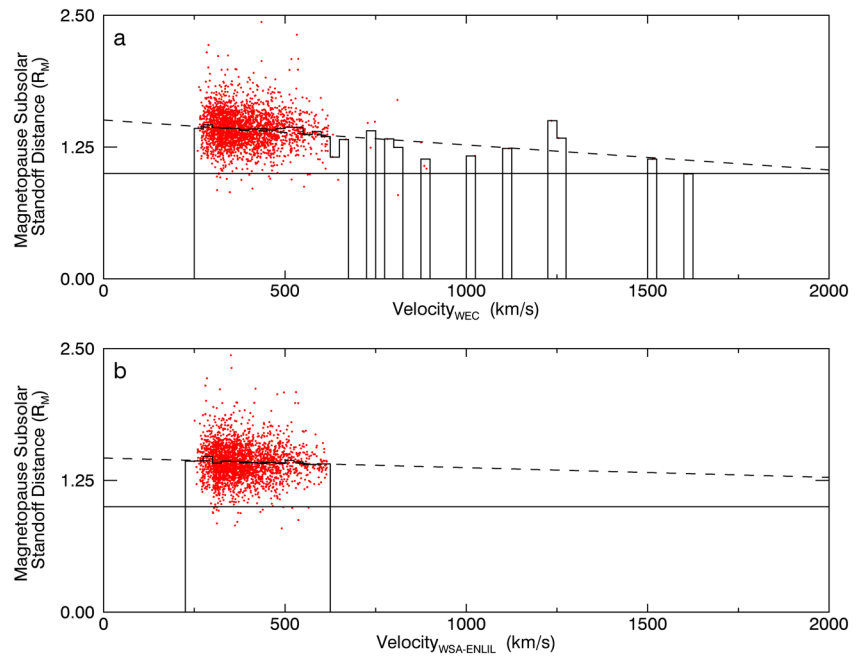
Figure 12. (a) Relation between mean magnetopause standoff distance (in units of Mercury radius R_M) and solar wind velocity computed from the WEC model. The dashed line shows the best linear fit to mean standoff distance versus velocity, and the solid horizontal line denotes Mercury's surface. The black histogram shows the standoff distance versus binned solar wind velocity. (b) Relation between the mean magnetopause standoff distance and solar wind velocity computed from the WSA-ENLIL model. Correlation coefficients are given in Table 2.

0.70, respectively. There are likewise strong correlations between MDI and residual model IMF strength δB, depicted in Figure 13b. MDI correlates well with binned δB for both models (both correlation coefficients are 0.99), but unbinned δB correlates more strongly for the WEC model at $r = 0.23$ versus $r = 0.12$ for the WSA-ENLIL model.

Finally, there are strong positive correlations between MDI and binned interplanetary electric field ($r = 0.85$) in Figure 13c. As found by *Baker et al.* [2013], the strength of these correlations results from a few extreme VB_S values; the majority of MDI values fall in the E range 1–10 mV/m. Neither correlation with unbinned observations, however, is significant, although both factors in the VB_S product (i.e., V and B individually) yielded strong correlations for both unbinned and binned parameter values.

4.3. Energetic Particle Intensity: Energetic Electron Burst Events

As a third indicator of the predictability and reliability of our models, we selected data on energetic electron bursts. We used the simpler, more robust data on such events from MESSENGER's NS over the EPS events analyzed by *Ho et al.* [2012]. Figure 14 shows the count rate of the energetic electron burst data [*Ho et al.*, 2011, 2012] versus ENLIL solar wind velocity V and IMF strength B. Similar to the other indicators, the Cone extension improves the correlation between the modeled velocity and the NS count rate by incorporating CMEs into the simulation of the inner heliosphere. The coefficient of correlation for unbinned values rises from $r = 0.09$ to $r = 0.11$, but that for binned values rises from $r = 0.42$ to $r = 0.60$, seen in Figure 14a. Figure 14b depicts NS count rate versus ENLIL IMF strength B. From experience at Earth, we would anticipate that strong magnetic reconnection between the IMF and planetary magnetosphere would cause substorms and particle bursts; a southward IMF (favoring stronger reconnection) more strongly correlates with burst data. As seen in Figure 6, ENLIL IMF angle distributions are more depleted than the angle distributions measured by MAG, preventing us from accurately isolating southward IMF from the models alone. *DiBraccio et al.* [2013] found, however, that the magnetopause reconnection rate at Mercury is independent of the IMF shear angle, so we examined the complete data set for modeled B. Correlated against B, the count rates show considerable scatter, but the binned data show stronger correlations, primarily with the WEC model ($r = 0.74$). We would expect the Cone extension to improve the correlation since a stronger IMF magnitude would increase reconnection rates, especially in this case of angle independence.
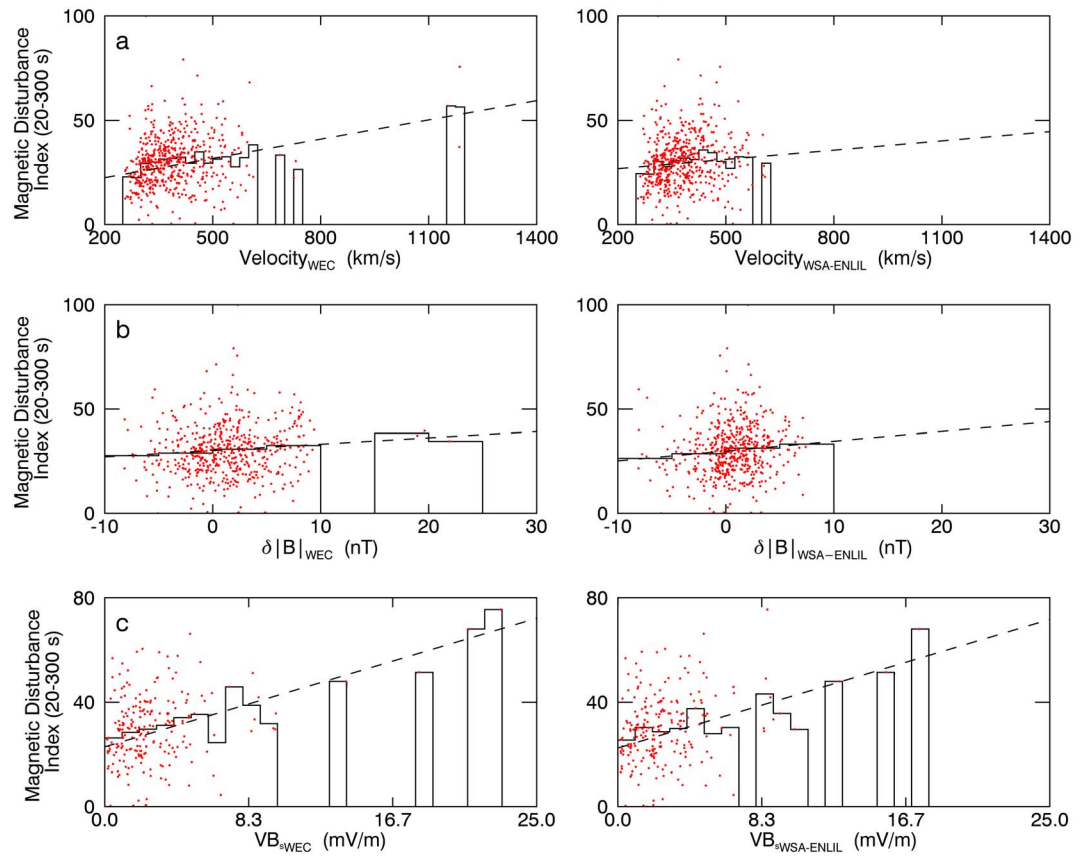
Figure 13. Comparison of magnetospheric indices with model parameters. (a) Mean values of low-frequency (20–300 s period) magnetic disturbance index (MDI) versus solar wind velocity from the (left) WEC and (right) WSA-ENLIL models. (b) Mean low-frequency MDI values versus background-corrected IMF strength (δB) from ENLIL. (c) Mean low-frequency MDI values versus interplanetary electric field strength VB_S (shown in Figure 9). The dashed lines show the linear fits, and the black histograms show the binned model parameters.
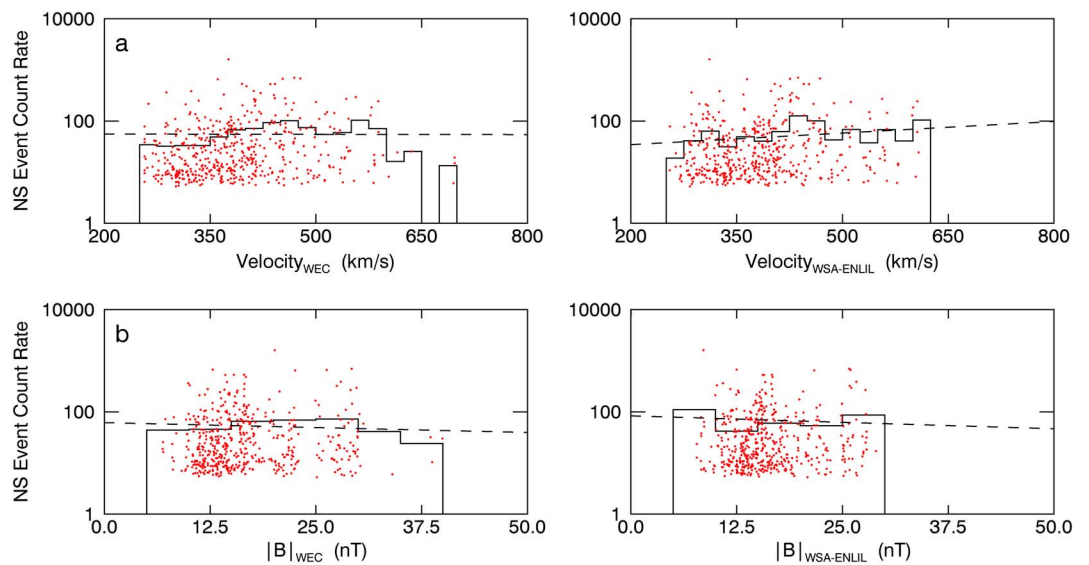
Figure 14. Comparison of magnetospheric indices with model parameters. (a) Count rate (logarithmic scale) of energetic electron burst events ($\geq$20 keV energy) versus solar wind velocity from the (left) WEC and (right) WSA-ENLIL models. (b) Count rate (logarithmic scale) of energetic electron burst events versus IMF strength from ENLIL. The dashed lines show the linear fits, and the black histograms show the binned model parameters.

5. Discussion and Conclusions

In this paper we expanded on earlier solar weather modeling at Mercury's orbital location [*Baker et al.*, 2013] by including transient solar events over the period from March 2011 to December 2012. We compared both the ambient solar wind modeling tool WSA-ENLIL and the extended, total solar wind tool WEC against direct solar wind and IMF measurements from the MESSENGER spacecraft. The MAG and FIPS instruments provided IMF and plasma measurements, respectively, for comparison. As noted above, the FIPS instrument could not readily sample the solar wind plasma distribution because of instrument placement and spacecraft orientation, but new retrieval methods [*Gershman et al.*, 2012] provided improved solar wind speed and temperature estimates.

Our comparisons between the models and in situ data show generally good agreement for both solar wind and IMF parameters. The WSA-ENLIL model matches the typical solar wind conditions accurately and reliably [*Baker et al.*, 2013], but the WEC model matches the total conditions better by incorporating CMEs and related transient solar events. Although the WSA-ENLIL model agrees with the baseline IMF strength (B) observed by the MESSENGER Magnetometer, the WEC extension can broadly reproduce the major deviations caused by CMEs and related events well, although the predicted arrival time for such simulated events can differ from the actual value by as much as several hours. Whereas the WEC model does not appear to mispredict event arrival time with any systematic offset, the WEC model systematically underpredicts the peak IMF strength of these solar events, likely because no magnetic cloud is included in the model. Although the WEC extension matches IMF strength well at other times, neither the WEC model nor the basic WSA-ENLIL model reliably predicts IMF vector angles, a recognized limitation of the models. Modeled versus actual solar wind speed (V) follows the same trend as for IMF strength: WSA-ENLIL fits the baseline speed well, but the Cone extension improves the modeling by including transient events. Remaining discrepancies between MESSENGER instruments and the WEC results can be attributed to microscopic processes not included in the model, differences in time resolution between the model and MESSENGER measurements, and CME arrival time errors (an ongoing challenge in heliospheric modeling).

Compared with solar wind modeling at Earth's orbital location, WEC and WSA-ENLIL more accurately predict IMF conditions at Mercury. Both solar wind models produce stronger correlations with the observed IMF strength at Mercury than at Earth when the results from this study are compared with those from previous studies. The RMS error in shock arrival time at Mercury, approximately 3 h, is also improved over the 8 to 12 h RMS error at Earth. These results are not surprising, however, since Mercury is closer to the inner ENLIL boundary where solar wind conditions are initialized.

In addition to solar wind parameter comparisons, we utilized magnetosphere and exosphere observations to further assess the predictability and accuracy of the models. We correlated magnetopause standoff distance, magnetospheric activity levels, and energetic particle burst properties against WEC and WSA-ENLIL parameters. Whereas *Baker et al.* [2013] used such observations primarily to show the utility of the WSA-ENLIL model in organizing MESSENGER results, we have shown here that the Cone extension improves the ordering and organizing of these results and thus WEC outperforms the standard WSA-ENLIL model. Most notably, the Cone extension improves the correlations with solar wind velocity. This result suggests that solar wind velocity is most amenable to improvement with the Cone extension among the parameters considered.

We conclude that modeling tools originally intended for Earth-based space weather forecasting can have more general applications. As we have shown with Mercury and the MESSENGER spacecraft, the models can help fill in data gaps in heliospheric observations and provide contextual information to planetary studies. With gaps in MESSENGER's in situ data record, specifically, we can use the space weather model to develop solar wind forcing functions such as those developed by *Borovsky* [2013] at Earth. Developing such solar wind forcing functions, however, will require more basic research on the solar wind-magnetosphere-exosphere coupling of the Mercury system. Since WSA-ENLIL+Cone model values can be specified throughout the inner heliosphere, model results can be used in conjunction with other planetary observations and campaigns. With MAVEN's campaign at Mars, for instance, WSA-ENLIL + Cone can provide space weather predictions and context to that mission [*Jakosky*, 2014]. As a general matter, in agreement with the findings of *Baker et al.* [2013], the work reported here demonstrates that solar wind modeling can beneficially unite heliospheric and planetary sciences.

References

Alexeev, I. I., et al. (2010), Mercury's magnetospheric magnetic field after the first two MESSENGER flybys, *Icarus*, *209*, 29–39, doi:10.1016/j.icarus.2010.01.024.

Anderson, B. J., M. H. Acuña, D. A. Lohr, J. Scheifele, A. Raval, H. Korth, and J. A. Slavin (2007), The Magnetometer instrument on MESSENGER, *Space Sci. Rev.*, *131*, 417–450.

Anderson, B. J., M. H. Acuña, H. Korth, M. E. Purucker, C. L. Johnson, J. A. Slavin, S. C. Solomon, and R. L. McNutt Jr. (2008), The structure of Mercury's magnetic field from MESSENGER's first flyby, *Science*, *321*, 82–85.

Anderson, B. J., et al. (2010), The magnetic field of Mercury, *Space Sci. Rev.*, *152*, 307–339.

Anderson, B. J., C. L. Johnson, H. Korth, R. M. Winslow, J. E. Borovsky, M. E. Purucker, J. A. Slavin, S. C. Solomon, M. T. Zuber, and R. L. McNutt Jr. (2012), Low-degree structure in Mercury's planetary magnetic field, *J. Geophys. Res.*, *117*, E00L12, doi:10.1029/2012JE004159.

Andrews, G. B., et al. (2007), The Energetic Particle and Plasma Spectrometer instrument on the MESSENGER spacecraft, *Space Sci. Rev.*, *131*, 523–526.

Arge, C. N., and V. J. Pizzo (2000), Improvement in the prediction of SW conditions using near-real-time solar magnetic field updates, *J. Geophys. Res.*, *105*, 10,465–10,479, doi:10.1029/1999JA000262.

Arge, C. N., J. G. Luhmann, D. Odstrcil, C. J. Schrijver, and Y. Li (2004), Stream structure and coronal sources of the solar wind during the May 12th, 1997 CME, *J. Atmos. Sol. Terr. Phys.*, *66*, 1295–1309.

Baker, D. N., T. I. Pulkkinen, V. Angelopoulos, W. Baumjohann, and R. L. McPherron (1996), Neutral line model of substorms: Past results and present view, *J. Geophys. Res.*, *101*, 12,975–13,010, doi:10.1029/95JA03753.

Baker, D. N., et al. (2009), Space environment of Mercury at the time of the first MESSENGER flyby: Solar wind and interplanetary magnetic field modeling of upstream conditions, *J. Geophys. Res.*, *114*, A10101, doi:10.1029/2009JA014287.

Baker, D. N., et al. (2011), The space environment of Mercury at the times of the second and third MESSENGER flybys, *Planet. Space Sci.*, *59*, 2066–2074, doi:10.1016/j.pss.2011.01.018.

Baker, D. N., et al. (2013), Solar wind forcing at Mercury: WSA-ENLIL model results, *J. Geophys. Res. Space Physics*, *118*, 45–57, doi:10.1029/2012JA018064.

Belenkaya, E. S., I. I. Alexeev, J. A. Slavin, and M. S. Blokhina (2013), Influence of the solar wind magnetic field on the Earth and Mercury magnetospheres in the paraboloidal model, *Planet. Space Sci.*, *75*, 46–55, doi:10.1016/j.pss.2012.10.013.

Blomberg, L. G., and J. A. Cumnock (2004), On electromagnetic phenomena in Mercury's magnetosphere, *Adv. Space Res.*, *33*, 2161–2165, doi:10.1016/S0273-1177(03)00449-6.

Boardsen, S. A., J. A. Slavin, B. J. Anderson, H. Korth, D. Schriver, and S. C. Solomon (2012), Survey of coherent ~1 Hz waves in Mercury's inner magnetosphere from MESSENGER observations, *J. Geophys. Res.*, *117*, A00M05, doi:10.1029/2012JA017822.

Borovsky, J. E. (2013), Physics-based solar wind driver functions for the magnetosphere: Combining the reconnection-coupled MHD generator with the viscous interaction, *J. Geophys. Res. Space Physics*, *118*, 7119–7150, doi:10.1002/jgra.50557.

Delcourt, D. C., T. E. Moore, S. Orsini, A. Millilo, and J.-A. Sauvaud (2002), Centrifugal acceleration of ions near Mercury, *Geophys. Res. Lett.*, *29*(12), 1591, doi:10.1029/2001GL013829.

DiBraccio, G. A., J. A. Slavin, S. A. Boardsen, B. J. Anderson, H. Korth, T. H. Zurbuchen, J. M. Raines, D. N. Baker, R. L. McNutt Jr., and S. C. Solomon (2013), MESSENGER observations of magnetopause structure and dynamics at Mercury, *J. Geophys. Res. Space Physics*, *118*, 997–1008, doi:10.1002/jgra.50123.

Feng, X. S., Y. Zhang, W. Sun, M. Dryer, C. D. Fry, and C. S. Deehr (2009), A practical database method for predicting arrivals of "average" interplanetary shocks at Earth, *J. Geophys. Res.*, *114*, A01101, doi:10.1029/2008JA013499.

Feng, X., M. Zhang, and Y. Zhou (2014), A new three-dimensional solar wind model in spherical coordinates with a six-component grid, *Astrophys. J. Suppl. Ser.*, *214*, doi:10.1088/0067-0049/214/1/6.

Fisher, R. R., and R. H. Munro (1984), Coronal transient geometry, 1, The flare-associated event of 1981 March 25, *Astrophys. J.*, *280*, 428–439, doi:10.1086/162009.

Fry, C. D., M. Dryer, Z. Smith, W. Sun, C. S. Deehr, and S.-I. Akasofu (2003), Forecasting solar wind structures and shock arrival times using an ensemble of models, *J. Geophys. Res.*, *108*(A2), 1070, doi:10.1029/2002JA009474.

Gershman, D. J., T. H. Zurbuchen, L. A. Fisk, J. A. Gilbert, J. R. Raines, B. J. Anderson, C. W. Smith, H. Korth, and S. C. Solomon (2012), Solar wind alpha particles and heavy ions in the inner heliosphere, *J. Geophys. Res.*, *117*, A00M02, doi:10.1029/2012JA017829.

Goldsten, J. O., et al. (2007), The MESSENGER Gamma-Ray and Neutron Spectrometer, *Space Sci. Rev.*, *131*, 339–391.

Gressl, C., A. M. Veronig, M. Temmer, D. Odstrcil, J. A. Linker, Z. Mikić, and P. Riley (2013), Comparative study of MHD modeling of the background solar wind, *Solar Phys.*, *289*, 1783–1801, doi:10.1007/s11207-013-0421-6.

Hakamada, K., and S.-I. Akasofu (1982), Simulation of three-dimensional solar wind disturbances and resulting geomagnetic storms, *Space Sci. Rev.*, *31*, 3–70, doi:10.1007/BF00349000.

Ho, G. C., et al. (2011), MESSENGER observations of transient bursts of energetic electrons in Mercury's magnetosphere, *Science*, *333*, 1866–1868, doi:10.1126/science.121101.

Ho, G. C., S. M. Krimigis, R. E. Gold, D. N. Baker, B. J. Anderson, H. Korth, J. A. Slavin, R. L. McNutt Jr., and S. C. Solomon (2012), Spatial distribution and spectral characteristics of energetic electrons in Mercury's magnetosphere, *J. Geophys. Res.*, *117*, A00M04, doi:10.1029/2012JA017983.

Howard, R. A., D. J. Michels, N. R. Sheeley Jr., and M. J. Koomen (1982), The observation of a coronal transient directed at Earth, *Astrophys. J.*, *263*, L101–L104, doi:10.1086/183932.

Jakosky, B. M. (2014), The MAVEN mission to Mars: Exploring Mars' climate history, in Eighth International Conference on Mars, abstract 1330, Lunar and Planetary Institute, Houston, Tex.

Jian, L. K., C. T. Russell, J. G. Luhmann, P. J. MacNeice, D. Odstrcil, P. Riley, J. A. Linker, R. M. Skoug, and J. T. Steinberg (2011), Comparison of observations at ACE and Ulysses with ENLIL model results: Stream interaction regions during Carrington rotations 2016–2018, *Solar Phys.*, *273*, 179–203, doi:10.1007/s11207-011-9858-7.

Johnson, C. L., et al. (2012), MESSENGER observations of Mercury's magnetic field structure, *J. Geophys. Res.*, *117*, E00L14, doi:10.1029/2012JE004217.

Korth, H., B. J. Anderson, T. H. Zurbuchen, J. A. Slavin, S. Perri, S. A. Boardsen, D. N. Baker, S. C. Solomon, and R. L. McNutt Jr. (2011a), The interplanetary magnetic field environment at Mercury's orbit, *Planet. Space Sci.*, *59*, 2075–2085.

Korth, H., B. J. Anderson, J. M. Raines, J. A. Slavin, T. H. Zurbuchen, C. L. Johnson, M. E. Purucker, R. M. Winslow, S. C. Solomon, and R. L. McNutt Jr. (2011b), Plasma pressure in Mercury's equatorial magnetosphere derived from MESSENGER Magnetometer observations, *Geophys. Res. Lett.*, *38*, L22201, doi:10.1029/2011GL049451.

Korth, H., B. J. Anderson, C. L. Johnson, R. M. Winslow, J. A. Slavin, M. E. Purucker, S. C. Solomon, and R. L. McNutt Jr. (2012), Characteristics of the plasma distribution in Mercury's equatorial magnetosphere derived from MESSENGER Magnetometer observations, *Geophys. Res. Lett.*, *117*, A00M07, doi:10.1029/2012JA018052.

Le, G., P. J. Chi, X. Blanco-Cano, S. Boardsen, J. A. Slavin, and B. J. Anderson (2013), Upstream ultra-low frequency waves in Mercury's fore-shock region: MESSENGER magnetic field observations, *J. Geophys. Res. Space Physics*, *118*, 2809–2823, doi:10.1002/jgra.50342.

Lee, C. O., J. G. Luhmann, D. Odstrcil, P. J. MacNeice, I. de Pater, P. Riley, and C. N. Arge (2009), The solar wind at 1 AU during the declining phase of solar cycle 23: Comparison of 3D numerical model results with observations, *Solar Phys.*, *254*, 115–183, doi:10.1007/s11207-008-9280-y.

Lee, C. O., C. N. Arge, D. Odstrcil, G. Millward, V. Pizzo, J. M. Quinn, and C. J. Henney (2013), Ensemble modeling of CME propagation, *Solar Phys.*, *285*, 349–368, doi:10.1007/s11207-012-9980-1.

Mays, M. L., et al. (2015), Ensemble modeling of CMEs using the WSA-ENLIL+Cone model, *Solar Phys.*, doi:10.1007/s11207-015-0692-1.

Odstrcil, D. (2003), Modeling 3-D solar wind structure, *Adv. Space Res.*, *32*, 497–506, doi:10.1016/S0273-1177(03)00332-6.

Odstrcil, D., V. J. Pizzo, J. A. Linker, P. Riley, R. Lionello, and Z. Mikic (2004a), Initial coupling of coronal and heliospheric numerical magnetohydrodynamic codes, *J. Atmos. Sol. Terr. Phys.*, *66*, 1311–1326, doi:10.1016/j.jastp.2004a.04.007.

Odstrcil, D., P. Riley, and X. P. Zhao (2004b), Numerical simulation of the 12 May 1997 interplanetary CME event, *J. Geophys. Res.*, *109*, A02116, doi:10.1029/2003JA010135.

Pizzo, V., G. Millward, A. Parsons, D. Biesecker, S. Hill, and D. Odstrcil (2011), Wang-Sheeley-Arge-ENLIL cone model transitions to operations, *Space Weather*, *9*, S033004, doi:10.1029/2011SW000663.

Raines, J. M., J. A. Slavin, T. H. Zurbuchen, G. Gloeckler, B. J. Anderson, D. N. Baker, H. Korth, S. M. Krimigis, and R. L. McNutt Jr. (2011), MESSENGER observations of the plasma environment near Mercury, *Planet. Space Sci.*, *59*, 2004–2015, doi:10.1016/j.pss.2011.02.004.

Raines, J. M., et al. (2012), Distribution and compositional variations of plasma ions in Mercury's space environment: The first three Mercury years of MESSENGER observations, *J. Geophys. Res.*, *118*, 1604–1619, doi:10.1029/2012JA018073.

Rouillard, A. P., et al. (2009), A solar storm observed from the Sun to Venus using the STEREO, Venus Express, and MESSENGER spacecraft, *J. Geophys. Res.*, *114*, A07106, doi:10.1029/2008JA014034.

Schatten, K. H., J. M. Wilcox, and N. F. Ness (1969), A model of interplanetary and coronal magnetic fields, *Solar Phys.*, *6*, 442–455, doi:10.1007/BF00146478.

Shue, J.-H., J. K. Chao, H. C. Fu, C. T. Russell, P. Song, K. K. Khurana, and H. J. Singer (1997), A new functional form to study the solar wind control of the magnetopause size and shape, *J. Geophys. Res.*, *102*, 9497–9511, doi:10.1029/97JA00196.

Slavin, J. A., et al. (2009), MESSENGER observations of magnetic reconnection in Mercury's magnetosphere, *Science*, *324*, 606–610.

Slavin, J. A., et al. (2010), MESSENGER observations of extreme loading and unloading of Mercury's magnetic tail, *Science*, *329*, 665–668, doi:10.1126/science.1188067.

Slavin, J. A., et al. (2014), MESSENGER observations of Mercury's dayside magnetosphere under extreme solar wind conditions, *J. Geophys. Res. Space Physics*, *119*, 8087–8116, doi:10.1002/2014JA020319.

Sundberg, T., et al. (2012), MESSENGER observations of depolarization events in Mercury's magnetotail, *J. Geophys. Res.*, *117*, A00M03, doi:10.1029/2012JA017756.

Sundberg, T., S. A. Boardsen, J. A. Slavin, V. M. Uritsky, B. J. Anderson, H. Korth, D. J. Gershman, J. M. Raines, T. H. Zurbuchen, and S. C. Solomon (2013), Cyclic reformation of a quasi-parallel bow shock at Mercury: MESSENGER observations, *J. Geophys. Res. Space Physics*, *118*, 6457–6464, doi:10.1002/jgra.50602.

Taktakishvili, A., A. Pulkkinen, P. MacNeice, M. Kuznetsova, M. Hesse, and D. Odstrcil (2011), Modeling of coronal mass ejections that caused particularly large geomagnetic storms using ENLIL heliosphere cone model, *Space Weather*, *9*, S06002, doi:10.1029/2010SW000642.

Tóth, G., et al. (2005), Space Weather Modeling Framework: A new tool for the space science community, *J. Geophys. Res.*, *110*, A12226, doi:10.1029/2005JA011126.

Tóth, G., et al. (2012), Adaptive numerical algorithms in space weather modeling, *J. Comp. Phys.*, *231*, 870, doi:10.1016/j.jcp.2011.02.006.

Vasyliunas, V. M. (2013), Role of the solar wind in the structure and dynamics of magnetospheres, in *Solar Wind 13: Proceedings of the 13th International Solar Wind Conference*, edited by G. P. Zank et al., *AIP Conference Proceedings*, vol. 1539, pp. 376–381, American Institute of Physics, Melville, N. Y., doi:10.1063/1.4811064.

Wang, Y.-M., and N. R. Sheeley Jr. (1992), On potential field models of the solar corona, *Astrophys. J.*, *392*, 310–319.

Winslow, R. M., B. J. Anderson, C. L. Johnson, J. A. Slavin, H. Korth, M. E. Purucker, D. N. Baker, and S. C. Solomon (2013), Mercury's magnetopause and bow shock from MESSENGER Magnetometer observations, *J. Geophys. Res. Space Physics*, *118*, 2213–2227, doi:10.1002/jgra.50237.

Xie, H., L. Ofman, and G. Lawrence (2004), Cone model for halo CMEs: Applications to space weather forecasting, *J. Geophys. Res.*, *109*, A03109, doi:10.1029/2003JA010226.

Zelenyi, L., M. Oka, H. Malova, M. Fujimoto, D. Delcourt, and W. Baumjohann (2007), Particle acceleration in Mercury's magnetosphere, *Space Sci. Rev.*, *132*, 593–609, doi:10.1007/s11214-007-9169-3.

Zhao, X. P., S. P. Plunkett, and W. Liu (2002), Determination of geometrical and kinematical properties of halo coronal mass ejections using the cone model, *J. Geophys. Res.*, *107*(A8), 1223, doi:10.1029/2001JA009143.

Zurbuchen, T. H., G. Gloeckler, J. C. Cain, S. E. Lasley, and W. Shanks (1998), A low-weight plasma instrument to be used in the inner heliosphere, in *Conference on Missions to the Sun II*, edited by C. M. Korendyke, *Proceedings of the Society of Photo-Optical Instrumentation Engineers*, vol. 3442, pp. 217–224, Bellingham, Wash.